Numerical and Experimental Studies on Choked Underexpanded Jets

By

Takuya MATSUDA*, Yoshikuni UMEDA*, Ryuji ISHII*,
Atsuhiko YASUDA* and Keisuke SAWADA**

(Received September 30, 1986)

Abstact

Axisymmetric underexpanded supersonic jets are investigated numerically and experimentally. A time-dependent technique of solution is applied to solve the Euler equations for a compressible ideal gas. The characteristics of the Mach disk obtained by the numerical calculations are compared with the experiments, and a good agreement is obtained.

It is shown that the numerical results are very sensitive to the choice of the boundary conditions imposed on the artificially introduced numerical boundaries. The boundary condition giving the best results is found to be the ambient gas condition.

It is shown that the global jet structure with a nearly regular shock pattern, wich is stable and steady itself, is destabilized by the vortex rings (Kelvin-Helmholtz roll-up) on the jet boundary. These vortices produce shocks inside the jet, which are convected downstream with the eddies. This strongly suggests that a time-independent or a time-converged solution cannot be expected without making a suitable time-averaging of the time-dependent solutions.

1. Introduction

Supersonic gas jets are popular in aeronautics and astrophysics. Typical examples are laboratory jets, jets exhausted from aircrafts and spacecrafts in aeronautics, and jets from galaxies and from cometary nuclei in astrophysics. Since the first laboratory study was done a century ago by Mach and Salcher, a large number of experimental and theoretical studies treating supersonic free-jets have been reported.

In general, a few kinds of discontinuities appear in a flow field of a jet expanded into a low pressure ambient gas. These are shock waves, jet boundaries and slip lines. The latter two are contact discontinuities. The strong shock

* Department of Aeronautical Engineering, Kyoto University, Kyoto 606, Japan
** Aircraft Engineering Division, Kawasaki Heavy Industries Ltd., Kakamigahara 504, Japan

waves are responsible for a spatially alternate appearance of supersonic and subsonic flow regions. The contact surfaces are responsible for the occurrence of Rayleigh-Taylor and/or Kelvin-Helmholtz instability.

Such discontinuities, therefore, introduce serious mathematical difficulties for a theoretical approach. Although the qualitative characteristics of supersonic free-jets have been well understood, theoretical predictions of detailed flow structures are not always satisfactory even now, and are often almost impossible in some complicated situations.

Recently, however, the development of super computers has provided us with a powerful tool for numerical investigations of the supersonic free-jet flows. For example, Norman et al.[1-3] have carried out extensive numerical simulations of astrophysical supersonic jets by the super computer CRAY-1. They have succeeded in showing some important analogies between the flow characteristics of the terrestrial and the astrophysical jets. Following the Blandford and Rees model[4] for radio jets exhausted from galaxies, Norman et al. modeled the astrophysical jets by pressure matched jets or density jets.

Obviously such jets are only special cases of the supersonic jets encountered in aeronautics. In the present paper, underexpanded supersonic jets are investigated in detail within the context of continuum ideal gas dynamics. The Euler equations for compressible gas are solved by a time-dependent difference scheme. Emphasis is placed on steady or quasi-steady (oscillatory) jets contrary to Norman et al. The jets are expanded from a uniform sonic nozzle into a stagnant ambient gas.

For a choked underexpanded jet, the most important parameter characterizing the jet is the pressure ratio (the ratio of the jet gas pressure at the nozzle exit to that of the ambient). This ratio determines the global structure of the jet.

At a high Reynolds number, the supersonic free-jet is highly Kelvin-Helmholtz unstable. This instability is most critical on the jet boundary and usually results in the Kelvin-Helmholtz roll-up, which commences in a thin shear layer near the nozzle lip to produce eddies (vortex rings). The eddies are convected downstream by the jet flow. These eddies interact with an oblique shock at the end of a shock cell to produce pressure waves (sound waves). The resultant pressure waves propagate upstream in the ambient gas, and they perturb the jet boundary near the nozzle lip. In this way a feedback loop of perturbation is established.

From a numerical point of view, numerical errors involved in a scheme act as a kind of viscosity called "effective viscosity" even in the ideal gas calculations. Then, strictly speaking, the numerical results for the Euler equations by a

finite difference scheme are mesh dependent, because the "numerical Reynolds number" is mesh dependent.

As has been described previously, the upstream part of the supersonic free-jet is rather steady while the downstream part is very unsteady. This can be best illustrated by two schlieren photographs of a free-jet (Figs. 8 a, b). Fig. 8 a was taken with a rather long time exposure, 1 / 30 sec, while Fig. 8 b was taken with a very short time exposure, 1.1 μs. The flow field shown in Fig. 8 b seems to be very turbulent compared with that in Fig. 8 a. The flow pattern shown in Fig. 8 b is an instantaneous one, while that in Fig. 8 a is to be considered as a mean flow field. (See also van Dyke[5].)

Such a situation suggests that a completely time-converged solution independent of the mesh size cannot be expected in the numerical calculations. Only if one uses a rather coarse mesh or introduces too much artificial viscosity, a seemingly steady solution is obtained. Then, it is useful to introduce the notion of a "quasi-steady" or a "quasi-converged" solution in the numerical calculations. In this paper, a suitable time averaging is used. This time averaged solution should be compared with the "exmerimental result", such as in Fig. 8 a. It was found that the time averaged solution was almost steady or slightly oscillating, and simulated fairly well the actual jet.

The second-order Osher scheme used in the present work has no explicit artificial viscosity to stabilize the solution. It was found that the numerical results were very sensitive to the choice of boundary conditions imposed on the numerical bondaries. Several kinds of boundary conditions on the numerical boundaries were tested. It was found that the ambient gas condition proposed by Sawada et al.[6] gave the best results.

In order to check the validity of the present code, some characteristics of the first Mach disk were computed and compared with experiments, and a good agreement was obtained. The present calculations were carried out on the super computer Fujitsu VP 200 at the Data Processing Center of Kyoto University and by the Fujitsu VP 50 at the Nobeyama Radio Observatory. The theoretical maximum speed of the VP 200 is about 520 MFLOPS. According to a bench mark test, the sustained speed of the VP 200 is comparable to the Cray-XMP. The sustained speed of the VP 50 is about half of that of the VP 200.

2. Formulation

2. 1 Basic equations

The basic equation governing an axisymmetric ideal gas flow is written in the vector from as

$$\partial U/\partial t+\partial F/\partial x+\partial G/\partial y+S=0 \tag{1}$$

$$U=\begin{pmatrix}\rho\\ \rho u\\ \rho v\\ e\end{pmatrix}\quad F=\begin{pmatrix}\rho u\\ \rho u^2+p\\ \rho uv\\ (e+p)u\end{pmatrix}\quad G=\begin{pmatrix}\rho v\\ \rho uv\\ \rho v^2+p\\ (e+p)v\end{pmatrix}\quad S=y^{-1}\begin{pmatrix}\rho v\\ \rho uv\\ \rho v^2\\ (e+p)v\end{pmatrix} \tag{2}$$

Where t, x, y, ρ, p, e, u and v are the time, the axial distance, the radial distance, the density, the pressure, the total energy per unit volume, the axial velocity and the radial velocity, respectively. The equation of state is given by

$$p=(\gamma-1)[e-\frac{1}{2}\rho(u^2+v^2)], \tag{3}$$

where γ denotes the ratio of specific heats of the gas, and is fixed to be 1.4 in the present work.

2.2 Numerical scheme

The robustness of the numerical scheme is very important to compute the supersonic free-jet, since strong discontinuities present in the flow field have a tendency to destabilize the flow. The numerical scheme used in the present analysis is the second-order accurate Osher scheme (Osher and Chakravarthy[7,8]). The cell method is used rather than a conventional finite difference method.

The technique to achieve the second-order of accuracy in space is different from conventional schemes, and the averaging function proposed by van Albada et al.[9] is used. In order to achieve the second-order of accuracy in time, the flow quantities at the half time-step $t^{n+1/2}$ are evaluated using the non-conservative quantities $V^t=(\rho, u, v, p)$ in place of the conservative quantities defined in Eq. (2)[9]. The details of the scheme are given by Sawada et al.[6]

2.3 Initial and boundary conditions

Since we are mainly concerned with a steady or a quasi-steady (oscillatory) solution, the initial condition is not important from a numerical point of view, because the initial condition does not affect the numerical results at a later time. In the present calculation, we assume a uniform ambient gas at rest in the whole computational domain at $t=0$. The jet begins to blow at $t=0$ from the circular nozzle.

Since the present scheme does not include any explicit artificial viscosity to smear out disturbances, the numerical results are rather sensitive to the choice of

boundary conditions imposed on the numerical boundaries, which may produce or reflect undesirable or unrealistic disturbances to the main flow.

The computational domain considered in the present work is a cylindrical one, whose cross section is shown in Fig. 1. The boundaries, on which proper boundary conditions are imposed, are the axis *AB*, the downstream boundary *BC*, the side *CD*, the upstream boundary *DE* and the nozzle exit *AE*. The boundary conditions considered in the present work are the jet condition, the symmetry condition, the pressure condition, the outflow condition and the ambient gas condition, which are formulated below.

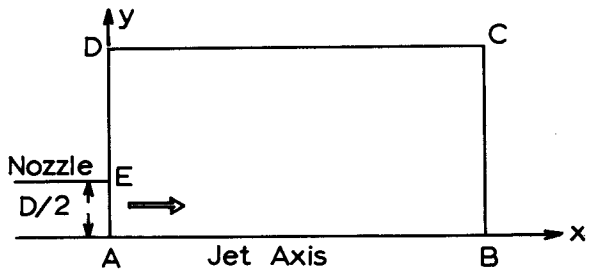

Fig 1. Sketch of the computational domain.

Since the physical variables are defined at the cell center in the cell method, we assume fictitious cells out of the boundaries. In these fictitious cells physical quantities are specified as described later. The fluxes just on the boundaries are computed by solving a Riemann problem between the state in the fictitious cell and that in the cell just inside of the boundary. This procedure seems to be slightly complicated, but it is not the case. When we compute all the cells including the fictitious cells, the proper boundary conditions are handled automatically. This is because the Riemann problems are solved at every cell and at every time step in the Osher scheme.

(a) Jet condition

The jet condition is given by

$$\rho_f=\rho_j,\quad p_f=p_j,\quad u_f=u_j,\quad v_f=v_j \tag{4}$$

where the subscripts f and j denote the fictitious cell and the jet gas condition at the nozzle exit. This condition is applied on the line *AE*.

In the present work, we specify the pressure ratio p_0/p_∞, where p_0 and p_∞ are the pressure of gas in the reservoir and of the ambient gas, respectively. The

temperature ratio T_0/T_∞ is fixed to be unity. The gas pressure at the nozzle exit is computed by the following formula assuming a quasi-one-dimensional flow:

$$p_j=p_0\,[1+(\gamma-1)M_j^2/2]^{-\gamma/(\gamma-1)}, \tag{5}$$

wheer M_j is the Mach number at the nozzle exit and is fixed to be unity in the present calculation.

(b) Symmetry condition

The symmetry condition is written as

$$\rho_f=\rho_i,\ p_f=p_i,\ u_{sf}=u_{si},\ u_{nf}=-u_{ni}, \tag{6}$$

where u_n and u_s are the velocity component normal to the boundary wall and the component tangential to the wall, respectively. The subscript i denotes the interior cell next to the boundary. This condition is applied on the jet axis AB, and it can be applied on a rigid wall, if any exists.

(c) Pressure condition

This is given by

$$\rho_f=\rho_i,\ p_f=p_\infty,\ u_f=u_i,\ v_f=v_i \tag{7}$$

The pressure in the fictitious cell is fixed to be an ambient value. This condition may be applied on the side CD.

(d) Outflow condition

We assume a type of valve on the surface, where the outflow condition is applied, and these valves permit only an outflow from the numerical domain to the exterior. This condition may be written as

$$\begin{aligned}&\rho_f=\rho_i,\ p_f=p_i,\ u_{sf}=u_{si},\ u_{nf}=u_{ni} \quad \textit{if}\ \ u_{ni}>0\\ &\rho_f=\rho_i,\ p_f=p_i,\ u_{sf}=u_{si},\ u_{nf}=-u_{ni} \quad \textit{if}\ \ u_{ni}<0.\end{aligned} \tag{8}$$

This condition may be applied on the surfaces BC and DE.

(e) Ambient gas condition[6]

In this condition, we assume that the fictitious cells are filled with an ambient gas in a fixed state. This can be written as

$$\rho_f=\rho_\infty,\ p_f=p_\infty,\ u_f=u_\infty,\ v_f=v_\infty. \tag{9}$$

This condition may be applied on the surfaces *BC*, *CD* and *DE*.

Obviously, the jet condition and the symmetry condition are reasonably applied on the nozzle exit *AE* and the symmetry axis *AB*, respectively. The conditions to be imposed on the other boundaries depend on the problem. When the boundaries *BC*, *CD* and *DE* are the numerical boundaries, as in the present analysis, the most suitable conditions applied on these boundaries should be determined rather ad hoc. In the present analysis, several combinations of the boundary conditions on the boundaries *BC*, *CD* and *DE* are tested, and important empirical information about the effects of the boundary conditions on the numerecal results was obtained.

3. Preliminary results based on the coarse grid

3.1 Check of the numerical code

In order to check the validity of the present numerical scheme, some of the characteristics of the first shock-cell structure are computed and compared with the experimental ones by Love et al.[10] It must be emphasized that, as will be shown later, the first shock–cell structure is very stable and steady, except for the cases of p_j/p_∞ close to unity. The numerical result of its structure does not appreciably depend on either the mesh size or the choice of numerical boundary conditions. Therefore, these quantities are suitable to check the validity of the numerical code.

Referring to Fig. 2, L is the distance from the nozzle exit to the Mach disk or the intersection of the incident shocks, S the diameter of the Mach disk, W the wave length, and D the diameter of the nozzle exit.

In Fig. 2, the numerical results for S/D, W/D and L/D are shown against the pressure ratio p_j/p_∞, and are compared with the experiments by Love et al.[10] In this figure, the circles denote the present numerical results and the solid lines denote the experiments by Love et al. As can be seen, the agreement between our numerical results and the experimental ones is excellent. This suggests that the present numerical scheme can well simulate the flow structure of a free–jet, at least in the upstream flow region.

3.2 Effect of numerical boundary condition on the result

As has been discussed in the introduction, the flow structure of a supersonic jet becomes gradually unstable with the increasing distance downstream. Then, the downstream part of the flow is time dependent or oscillatory. The numerical results, therefore, are influenced very much by the disturbances emanated or reflected from the numerical boundaries. In this respect, the choice of numerical

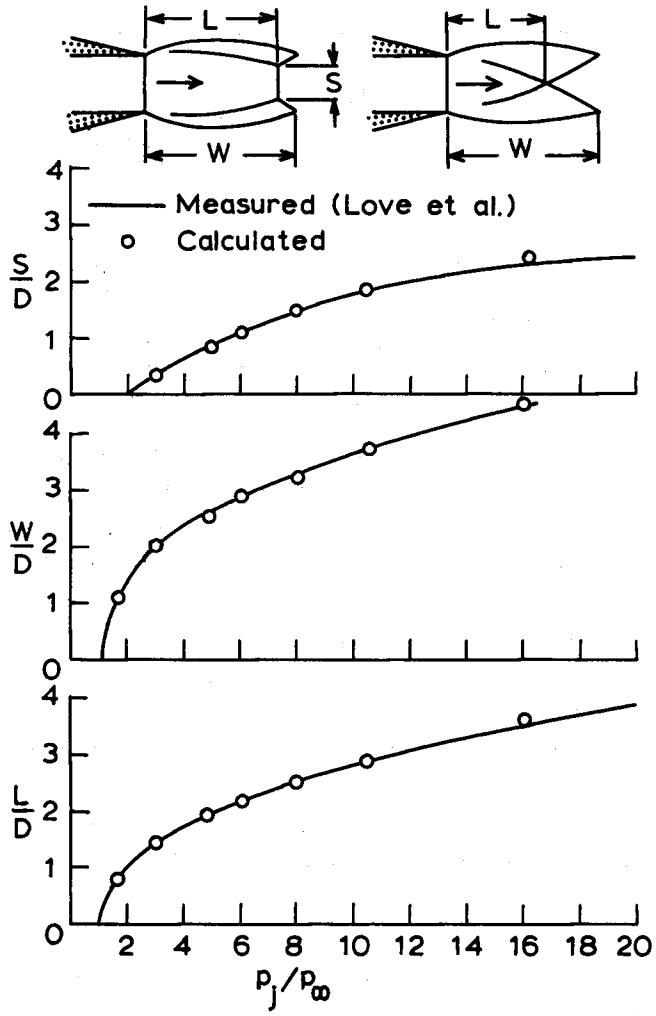

Fig 2. Sketch of the first shock-cell structure behind an underexpanded sonic nozzle (above). The comparison between our numerical results and Love et al.'s experiments[10] (below).

boundary conditions is very important.

Here, we will investigate in detail the effects of the numerical boundary conditions on the downstream part of the flow structure. Then, we will make an effort to find the most suitable set of numerical boundary conditions for the present experiments, where the uniform sonic air jet is expanded into the stagnant ambient air in a substantially large container or into a stagnant atmosphere.

Table 1.

Case	Boundary			
	BC	CD	DE	Grid
1	A	A	A	225 × 37
2	A	P	A	225 × 37
3	O	P	O	225 × 37
4	A	S	S	225 × 37
5	O	A	O	225 × 37
6	A	A	A	450 × 74

In the table *A*, *P*, *O* and *S* denote the amblient gas condition, the pressure condition, the outflow condition and the symmetry condition, respectively.

We present here the computed results of the jets with the pressure ratio $p_0/p_\infty = 3.90$ ($p_j/p_\infty = 2.06$). This pressure ratio is the threshold for the formation of the Mach disk. The computational space is 11.1 D long along the jet axis and 1.9 D long across it, where D is the nozzle diameter at the exit. The number of meshes is 225×37. The cases with numerical boundary conditions listed in Table 1 are computed and compared. One run takes 7 − 8 min/ 5000 steps by VP 200.

Figure 3 shows spacetime diagrams of the density along the symmetry axis. In the following figures, length, velocity and density are normalized by D, c_∞, and ρ_∞. The horizontal axis denotes the axial distance, while the vertical axis denotes the time. The dark blue shows the lower density, while the white shows the higher density. The edge where the color changes from dark blue to white abruptly is a shock. Case 6 shows the same case as Case 1 except for the finer mesh, i.e. 450 × 74.

After the jet begins to blow at t= 0, a weak shock wave is formed ahead of a contact surface. (These two features can be seen as two straight lines originating from the origin.) The shock wave propagates downstream much faster than the contact surface, which is the head of the jet. We may observe several steady vertical features, which are time stationary waves, i.e. the shock-cell structures. Behind the contact surface, the first shock-cell structure is formed in the early stage of the evolution. After that, the second, the third, etc.... shock-cell structures are formed successively in time. One may observe that a flow becomes a quasi-steady state shortly after the contact surface reaches the downstream boundary.

Case 1 is the best one, as will be discussed. This figure well demonstrates that the flow structure is not steady in a strict sense even at later time, especially in the downstream region. Fluctuations of relatively small scale are

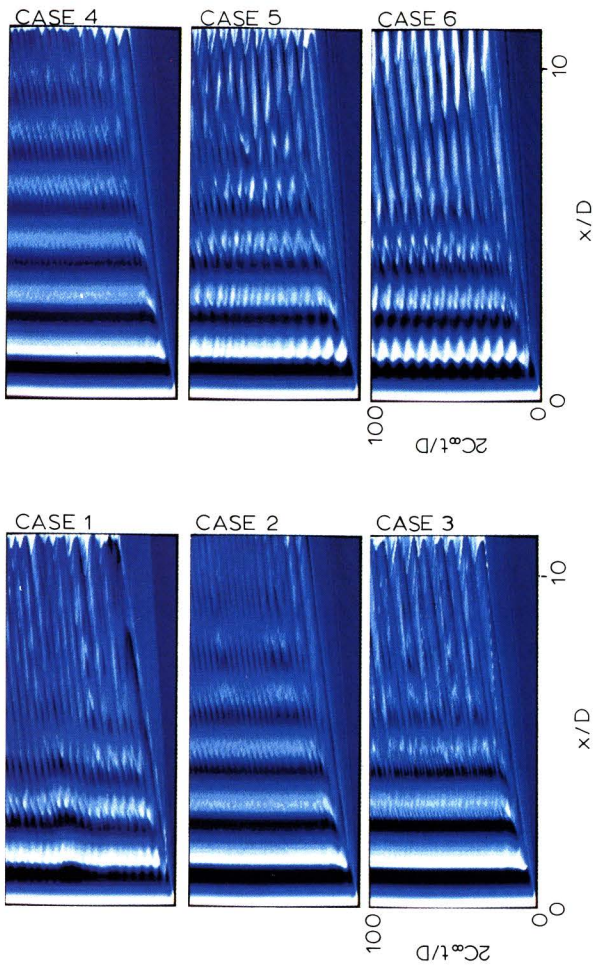

Fig 3. Spacetime diagrams of the density along the symmetry axis computed by using various types of boundary conditions shown in Table 1. The horizontal scale is space and the vertical axis is time. The maximum value of density is white, the minimum is dark blue, and the intermediate values are 12 shades of blue representing equal linear intervals between 2.4 and 0.75. The density of the unperturbed gas is unity. The shocks are located where the tone changes from dark to light abruptly. The vertical steady features are the quasi-steady shock-cell structures. One can see streaming motions which are periodic internal shocks produced by vortices convected downstream.

superimposed on the otherwise steady regular shock-cell structure. The amplitude of fluctuations becomes larger with the increasing axial distance downstream. The propagation speed and the time interval of occurrence of the fluctuations seem to have some regularity.

One of the most important facts to be noted in this figure is that a time-converged solution in the conventional sense cannot be expected at all, even at $t \to \infty$. Nevertheless, the time-averaged behavior of the density profile is clearly steady. Therefore, we have a quasi-steady or quasi-converged flow.

The result shown in Case 2 is for the boundary condition, where the ambient gas condition on the upper boundary in Case 1 is replaced by the pressure condition. There is an important difference between the results shown in Cases 1 and 2. In Case 2, the identity of the basic shock-cell structure in the downstream region is almost lost due to the superimposition of strong disturbances. One may observe disturbances propagating upstream as well.

Since such a difference comes from the boundary condition at the side, it can be said that the pressure condition emanates and/or reflects the disturbances more effectively than the ambient gas condition. This fact is best illustrated by the several pressure waves extending to just ahead of the jet front, except the frontal one. These waves are the reflected waves of the first weak shock from the side.

The fluctuations in the downstream flow are more enhanced in the result for Case 3, where the outflow condition is applied at *BC* and *DE*. In this case, even the first shock-cell system shows an appreciable scale of oscillation. This oscillatory motion interacts with the next downstream shock-cell structure to induce an even stronger oscillation. A similar condition to this was used by Norman et al. in the calculations of the astrophysical jets[1-3].

Physically, Case 4 corresponds to the jet expanded into an ambient gas in a semi-infinite cylindrical chamber. At an early stage, several rather strong pressure waves are seen to propagate downstream ahead of the jet front, as is in Cases 2 and 3. These waves, except the first one, are the pressure waves reflected from the rigid wall.

The result shown in Case 5 is for the boundary condition, where the pressure condition on the upper boundary in Case 3 is replaced by the ambient gas condition. This result is similar to that in Case 1. The shock-cell structure is, however, appreciably weakened with the increasing axial distance downstream. Although the flow region close to the numerical downstream boundary shows a dominant fluctuation, the magnitude of the fluctuation is by far smaller than that observed in Cases 2-4.

Case 6 shows the spacetime diagram of the flow with the same boundary condition as in Case 1, except for the finer grid, i.e. 450×74. In this figure, we can identify only the first four shock-cell structures rather well, while we can find six in Case 1. The fifth cell is barely visible. In the finer grid, the mesh Reynolds number is about four times larger than the coarser one, and therefore the flow is more unstable to the Kelvin-Helmholtz instability. This calculation agrees best with an experimental observation discussed later.

In this way, the numerical solution of the inviscid jet is mesh dependent. Therefore, one must be careful in comparing the numerical results with experimental ones in a quantitative manner. Nevertheless, we may draw useful information on the qualitative features of the jet from the calculations.

The density contours of the jets corresponding to the results in Fig. 3 are shown in Fig. 4 at an integration time step $n = 5000$. It is well demonstrated that the shock-cell structure of the jet for Case 1 is spatially most regular among others, and the sound field surrounding the jet is quiet.

It is worthwhile to mention that we have also tested other possible boundary conditions not discussed in the above. If we permit an inflow in the outflow condition, a supersonic inflow from the upstream end *DE* occurs, and the flow pattern obtained does not resemble the real one at all.

In order to estimate the physical variables in the fictitious cell, it is possible to extrapolate linearly from the interior values. If we adopt such a boundary condition on *DE*, the numerical time step becomes too small to continue the computation any further.

Summarizing the above discussion, we may conclude that the ambient gas condition is best for the side boundary *CD*, since the artificial reflection of waves is almost absent. As to the upstream end *DE*, both the ambient and the outflow conditions give similar results, at least as far as the present ploblem is concerned. They give slightly different results in the case of astrophysical jets, which will be discussed in a separate paper.

As far as the downstream end *BC* is concerned, the ambient gas and the outflow conditions give slightly different results. As was discussed in the above, the ambient gas condition gives a regular shock pattern. It seems strange to find this phenomenon, because we have a strong standing shock wave just in front of the end *BC* in the case of the ambient gas condition. This will be discussed later.

3.3 Feedback loop of generation of disturbances

Close investigation of the results in Figs. 3 and 4 will suggest that there is

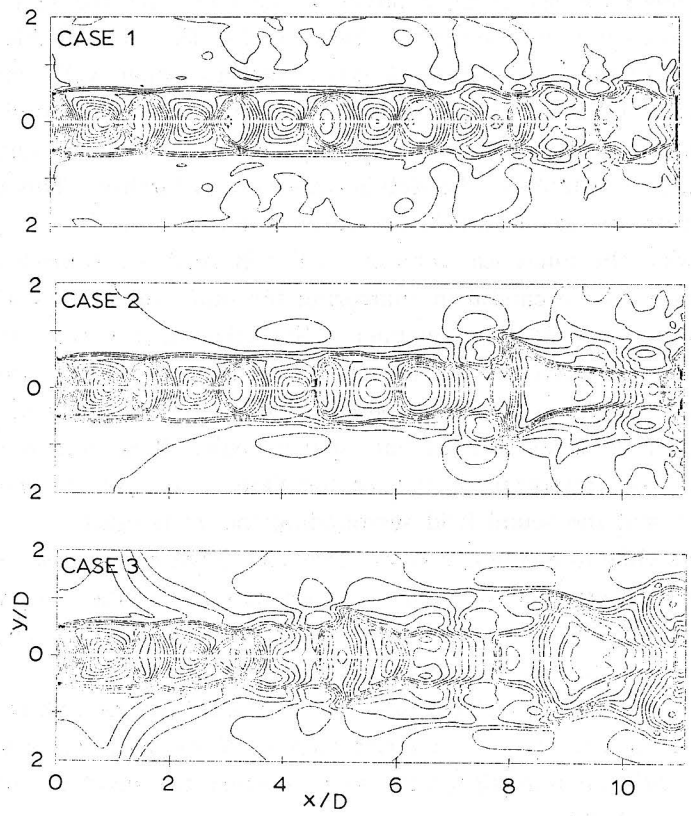

Fig 4. Density contours of the numerical solutions at $n=5000$, corresponding to each case shown in Fig 3. The pressure ratio is $p_0/p_\infty=3.90$ $(p_j/p_\infty=2.06)$.

a relation between the instability of the jet flow and the sound field surrounding the jet. It is quite reasonable to assume the presence of a feedback loop to exite the oscillation in the shock-cell structure. Such a mechanism was proposed by Powell[11, 12].

In the jet expanding in the stagnant atmosphere, there is a mechanism of generation of pressure waves (sound waves). At the rear edge of each shock-cell structure, the reflected shock intersects the jet boundary. At these points, sound waves are generated due to the interaction between the eddies and the shock waves. In the experiments, such pressure waves are observed as the "screech tone"[11, 12]. In Fig. 4, the pressure waves thus formed are seen to be propagating in the ambient.

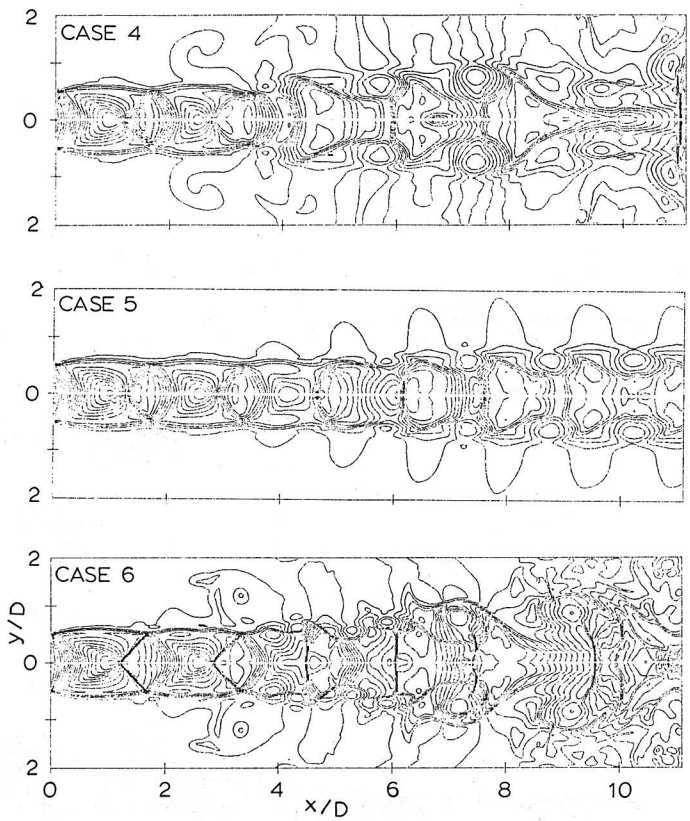

These runs use a 225 × 37 grid except Case 6 where a 450 × 74 grid is used. Contour lines are in equal linear intervals, 0.1, of density between the maximum and the minimum.

There is another (artificial) mechanism of generation of sound in the present calculation. Sound waves may be partly excited by the impingement of the coherent flow structure (the Kelvin–Helmholtz eddies) on the downstream end *BC*. Since the flow velocity in the jet is supersonic along the axial direction, the disturbances produced and/or reflected at the downstream region cannot propagate upstream through the jet, but through the ambient. Therefore, the boundary conditions assumed on the side *CD* and the upstream end *DE* take part in the feedback loop through the reflection of the pressure waves. As was shown in Case 4, the symmetric boundary can effectively reflect the waves escaping from the sound field surrounding the jet to infinity, thus influencing the reson-

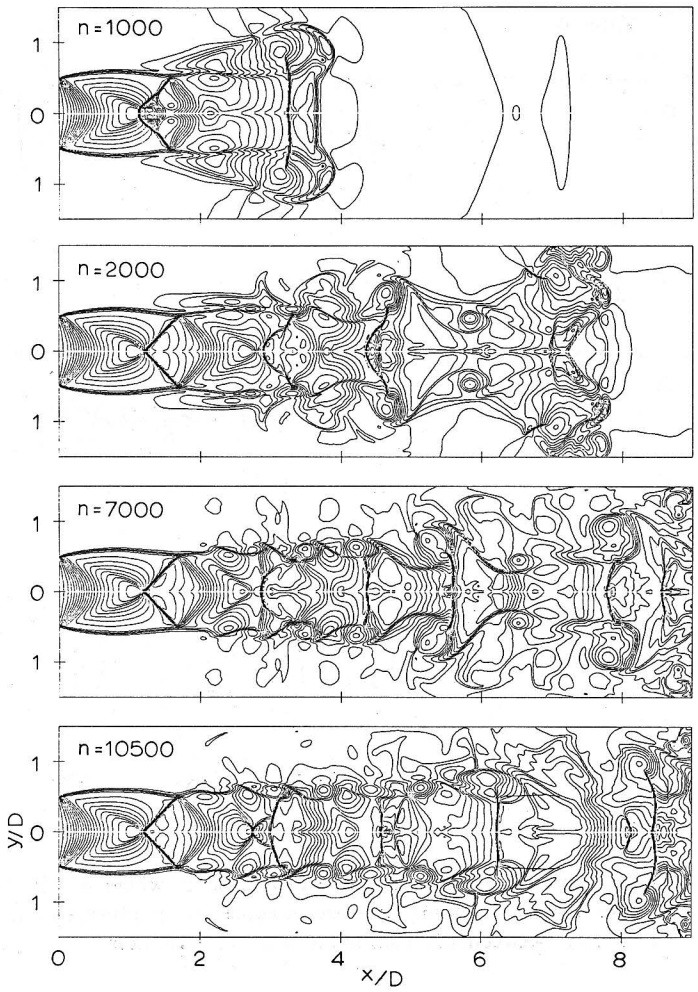

Fig 5. Time history of the same jet as shown in Figs. 3 & 4. This run uses a 450 × 74 grid and the Case 1 boundary condition. Early stage of the evolution before the jet front reaches the right boundary : $n=$ 1000, 2000. Quasi-steady or quasi-converged stage of the jet : $n=$ 7000, 10500.

ance. The pressure boundary condition on the side *CD* gives a similar effect as the symmetry condition, as was shown in Cases 2 and 3.

The present numerical results clearly show the existence of a strong resonance in the flow. The waves propagating upstream through the ambient gas

interact with the thin shear layer near the nozzle lip to excite the Kelvin-Helmholtz instability. The eddies thus formed are convected downstream to close the feedback loop.

As was discussed previously, the numerical results are strongly dependent on the choice of numerical boundary conditions. In what follows, only the ambient gas condition (Case 1 in Table 1) will be used in the numerical calculations. The physical meaning of this condition will be discussed again in connection with our experimental observations.

4. Numerical results based on the finer grid

So far, the effects of the boundary conditions on the numerical results based on the rather coarse mesh have been discussed in detail. Here, the jets computed on the finer grid, e.g. 450×74, are presented and investigated. The numerical region is $9D$ along the jet axis and $1.5D$ across it. Therefore, the mesh size is still finer than that in Case 6.

4.1 Early evolution of the jet and the shape of the jet front

In the present analysis, the jet begins to blow at $t=0$. After that, it penetrates through the ambient gas producing a normal shock, a contact surface and a pressure wave (a weak shock) ahead of the contact surface (the jet front). Figure 5 shows the time evolution of the density contours of the jet, whose parameter is the same as before. Although the pressure ratio is greater than unity, the shape of the penetrating front of the jet is very similar to that of the matched jet computed by Norman et. al[1-3].

On the frontal contact surface, which was called a working surface by Blandford and Rees[4], the Rayleigh-Taylor instability may occur if the working surface is accelerated. Since the penetrating speed of the contact surface is nearly constant, except for the very early stage, this instability may not be important. In spite of this, the working surface changes its shape appreciably with time. It emanates successively the pressure waves, which propagate faster than the contact surface, and soon overtake the wave front.

This instability (or oscillation) of the working surface is obviously not the Rayleigh-Taylor instability, but a Mach disk induced instability. The axial component of the flow velocity (and the momentum as well) of the gas downstream of the normal shock is smaller than that of the gas passing through the oblique shock reflected from the triple point. This difference in the axial momentum results in the deformation of the working surface looking like a Y-shape. The top of the Y-shaped working surface rolls up by the Kelvin-

Helmholtz instability, and thus changes the strength of the shocks. This feedback loop was fully discussed by Norman et al.[1-3]

This instability is, however, important only in a transient unsteady jet. At some stage, the working surface reaches the downstream boundary, and then goes away from the computational domain. After that, the disturbances produced at the unsteady head of the jet gradually decay with time. It is to be noticed that the shock-cell structure near the nozzle exit is formed relatively in an early stage of the evolution, and its global structure does not change with time.

4.2 Oscillatory and time-averaged jets

The first shock-cell structure seems to be quite stable and the global structure is almost completely time independent after the jet front reaches the right boundary. (See Fig. 3.) Only a very slight wavy motion of the jet boundary can be seen near the rear edge of the first cellular structure.

This wavy motion of the jet boundary is appreciably amplified when it passes through the reflected shock. On the jet boundary of the second cell, the amplified wavy motion is further enhanced to form a large ring vortex (Kelvin-Helmholtz roll-up). This ring vortex is convected downstream. When this ring vortex is convected some distance, another ring vortex is formed on the jet boundary of the second cell. This process is repeated at about every 150 integration steps.

Slightly downstream of the point where the second incident shock is reflected, a nearly normal shock is formed, and it interacts with the basic structure to form a complicated oscillatory shock system. This oscillatory motion of the shock system occurs periodically. (See Fig. 3.) The period of the oscillation is essentially the same as that of the production of ring vortex.

The scale length of the ring vortex in the third cell is almost comparable to

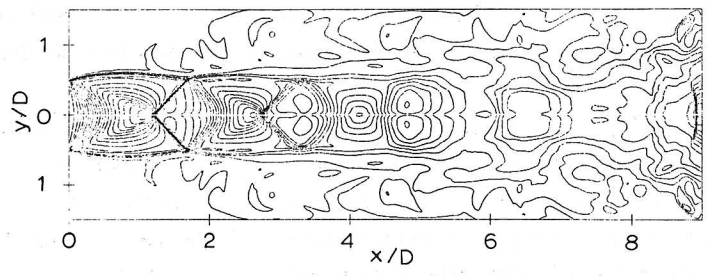

Fig 6. Time averaged density contour over 450 time steps from 10050 to 10500. The model parameter is the same as in Fig. 5.

the jet width, and therefore the flow structure of the third cell is quite unsteady. In spite of this, such an apparent complicated unsteady motion is repeated quite periodically in time, as can be seen in Fig. 3. The period of the oscillation in the third cell is about 450 time steps, and it is much longer than that in the second cell.

Figure 6 is the time averaged density contours over 450 time steps from 10050 to 10500. In the third cell of the time dependent jets, all the shocks are unsteady and nearly normal. Therefore, the third shock-cell structure in the averaged density contours in Fig. 6 is rather smeared out. On the other hand, the second shock-cell structure is retained fairly well in Fig. 6. It is interesting to note that the second reflected shock has no clear counterpart in the instantaneous flow field shown in Fig. 5. Only in the time averaged figure, this smeared reflected shock is observed. The jet boundary in the averaged flow is also very smooth. These facts are quite consistent with our observation in the long-time -exposure schlieren photograph to be discussed later.

Near the downstream boundary, an array of ring vortices are observed, and it perturbs the global structure of the shock-cells there. The region surrounded by a large ring vortex forms a sort of de Laval nozzle. (see Fig. 5.) The flow passing through this nozzle becomes supersonic. In many cases, such flow patterns are accompanied by normal shocks near the throat of the ring vortex. A repeated nozzle-shock structure observed in the present calculations is realized in this manner. Since the vortices are convected downstream by the main flow, the nozzle-shock patterns are also convected downstream. This mechanism is responsible for the streaming motion of the downstream part of the jets observed in the spacetime diagram of Fig. 3.

5. Experiments

5.1 Experimental apparatus

Schlieren photographs of the flow field were taken for various pressure ratios in order to investigate the flow characteristics of supersonic jets.

A choked underexpanded air jet was exhausted from a circular sonic nozzle with an internal diameter $D = 1.0$ cm. The nozzle geometry is shown in Fig. 7. The pressure ratio was regulated by a control valve.

For the flow visualization, the optics employed was a conventional schlieren setup, which was a single-path design with the optical axis folded twice by using two spherical mirrors, the diameters being 20 cm and the focal lengths being 200 cm. In the present experiments, two types of light sources were employed. For long-time-exposure (1 / 30 sec) schlieren photographs, a mercury

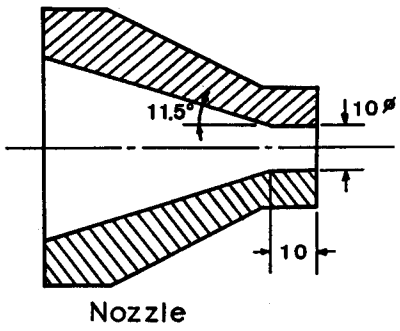

Fig 7. Sketch of the nozzle used in the present experiment.

discharge lamp which illuminates continuously was employed. For the instantaneous schlieren photographs, the light source was a stroboscopic flash unit having flash durations adjustable at $1.1-4.5\mu s$ at four discrete settings. We always set the flash duration at $1.1\mu s$ to take the instantaneous schlieren pohotographs. The controlling parameter for the jet was the stagnation pressure p_0, which varied between $1.0-6.0$ kg/cm^2.

5. 2 Experimental results and comparison with numerical results.

Samples of the long-time-exposure and the instantaneous photographs of the jet are shown in Figs. 8 a and 8 b, together with the computed density contours for the jet with the pressure ratio $p_0/p_\infty = 3.90$ $(p_j/p_\infty = 2.06)$. As can be seen, these two photographs seem to show completely different phenomena at a first glance. It is difficult to find any relation between the flow structures in the downstream region shown in these two photographs. The flow shown in the instantaneous photograph seems to be very fluctuated and turbulent, and the three-dimensional helical structure can be seen. It is very difficult to identify the third, and the fourth etc. shock-cell patterns seen in the long-time-exposure photograph.

On the other hand, the long-time-exposure photograph shows a rather smooth and regular shock-cell pattern. The butterfly pattern seen in the third and the fourth cells indicates that the shocks are oscillating along the jet axis as well as vertically.

In the present experiments, the shock pattern in the long-time-exposure photographs did not change its shape and location, even when the exposure time was varied from $1/1000\,s$ to $1/4\,s$. It suggests that the shock pattern seen in Fig. 8 a shows some time mean feature of the jet structure, and should be compared with the time averaged flow solution shown in Fig. 6.

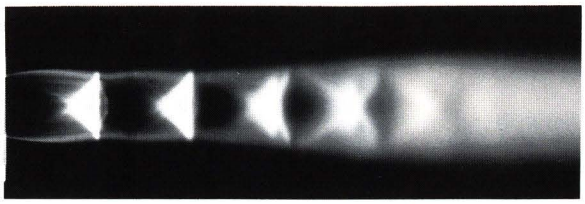

a

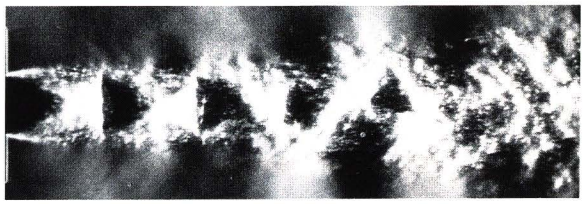

b

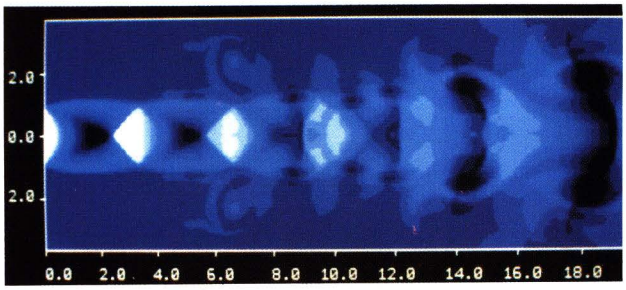

c

Fig 8. *a* A schlieren photograph of the jet with a long exposure time, i.e. 1/30 *s*. The parameter of the jet is the same as in Figs. 3, 4, 5 and 6. One can see mean shock-cell structures. Butterfly patterns seen in the third and the fourth cells show an unsteady motion of the shocks. *b* An instantaneous schlieren photograph with the exposure time 1.1 μs. It is difficult to identify the third, the fourth etc. shock-cells. Note sound waves surrounding the jet. A three-dimensional helical structure can be seen. *c* A blue scale of the calculated density.

5.3 Multiple exposures photograph

In order to find a relation between an instantaneous photograph and a long-time-exposure one, we took photographs with multiple exposures as shown in Fig. 9. Each flash duration is 1.1 μs, and the time interval between two successive flashes is about 1 *s*. The numbers of flashes are denoted in each

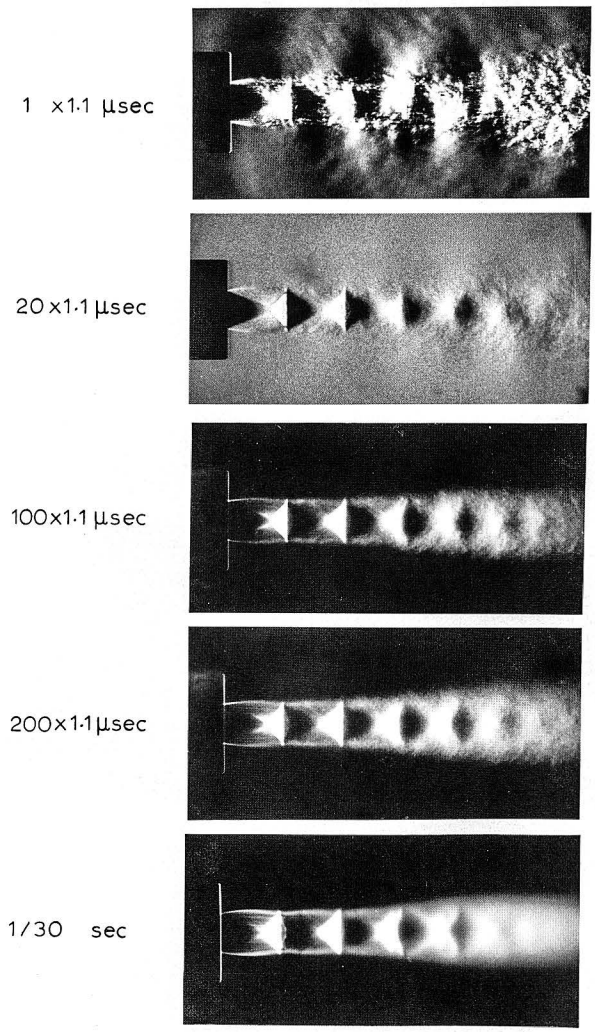

Fig 9. Multiple exposure schlieren photographs. Number of flashes with duration time 1.1 μs is shown in the figure.

photograph. With the increasing number of flashes, the shock pattern becomes clearer, and the sound field surrounding the jet becomes quieter. When the number of flashes is 200, the structure of the jet and the sound field are almost the same as those shown in the long-time-exposure photographs (bottom). Since the time interval of the two successive flashes is long enough, we may assume

that each flash was distributed uniformly in one cycle of the oscillation.

5.4 Jets with an obstacle inserted

When we apply the ambient gas condition at the downstream numerical boundary, we have a standing shock just in front of the boundary. It may be argued that this shock produces noisy sound waves, which propagate upstream to perturb the flow. Contrary to this expectation, we had a quieter flow in this case, as was discussed previously.

In order to investigate the role of the downstream boundary experimentally,

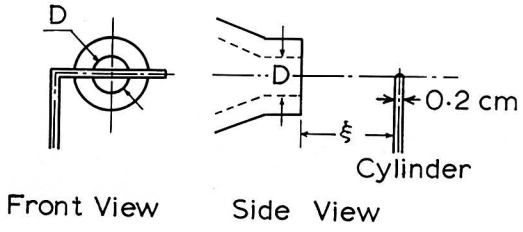

Fig 10. Sketch of the obstacle inserted in a jet.

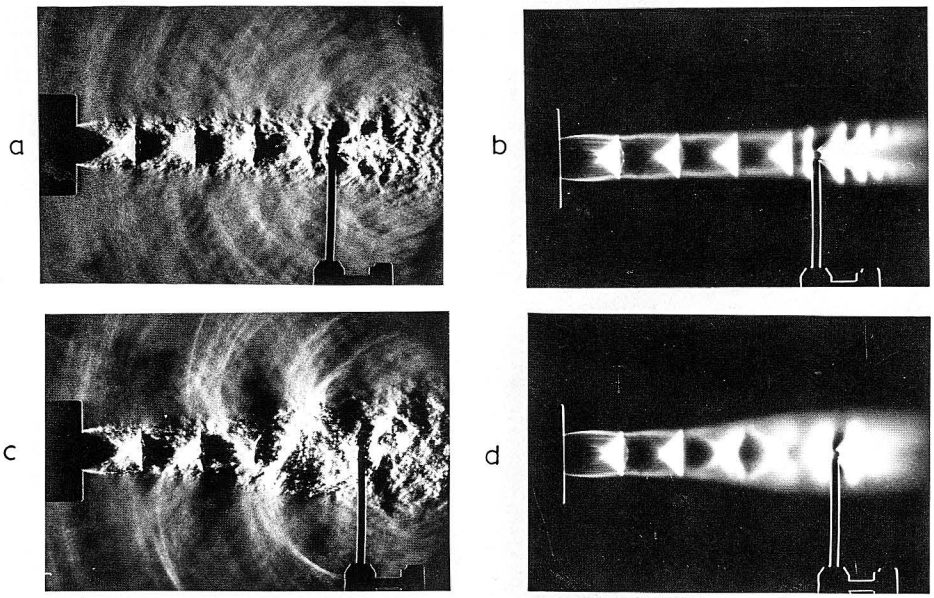

Fig 11. *a* An instantaneous schlieren photograph of the jet in which an obstacle is inserted at $\xi = 6.6\,cm$. *b* A long-time-exposure photograph of the above case. *c* An instantaneous schlieren photograph with $\xi = 7.2\,cm$. *d* A long-time-exposure potograph of case *c*.

we insert a Γ-shaped cylinder, as shown in Fig. 10, in the jet. The obstacle is placed perpendicularly to the jet axis through the center of a jet cross-section. The distance from the nozzle exit to the cylinder is denoted by ξ.

When the cylinder is inserted into the jet, a strong disturbance is produced by the impingement of the jet flow on the cylinder, and the jet is influenced. Figures 11 a, b, c, and d are the instantaneous schliern photographs and the long-time-exposure ones for $\xi = 6.6\,cm$ and $7.2\,cm$, respectively. It is interesting to note that the jet with an obstacle at $\xi = 6.6\,cm$ is very regular. It is actually even more stable than the case without an obstacle. (Compare Fig. 11 with Fig. 8.) On the other hand, the case with $\xi = 7.2\,cm$ is much more disturbed compared with the other cases.

The reason for this phenomenon may be explained as follows. The pressure

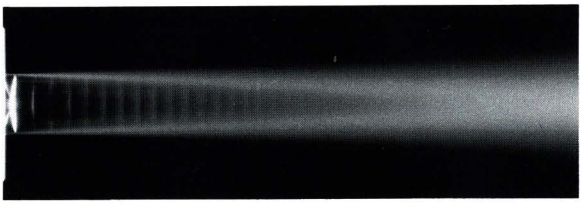

a

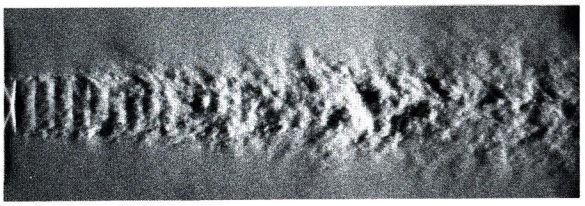

b

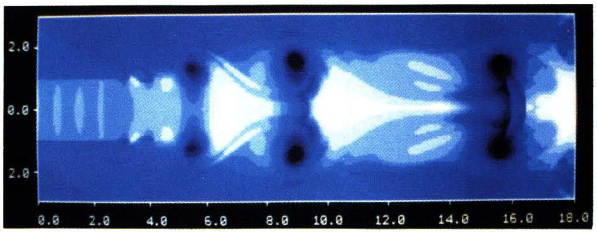

c

Fig 12. *a* A long-time-exposure schlieren photograph of the jet with $p_0/p_\infty = 1.99$ ($p_i/p_\infty = 1.05$). *b* An instantaneous photograph. *c* A blue scale of the calculated density.

waves produced at the cylinder propagate upstream through the ambient gas to form a feedback loop, as was discussed before. One of the key factors in this feedback loop is phase matching. The frequency of the sound wave thus produced is determined by the frequency of the passage of vortices through the downstream end. The sound propagating upstream interferes with the jet at the rear edge of the shock-cells. If this interference is in phase, then we have a disturbed flow. On the other hand, if the interference is out of phase, a quiet flow results. Therefore, the distance ξ determines the character of the flow. Although the phenomena discussed above are intersting, they are out of the scope of the present paper and will be discussed elsewhere.

5.5 Jets with various pressure ratios

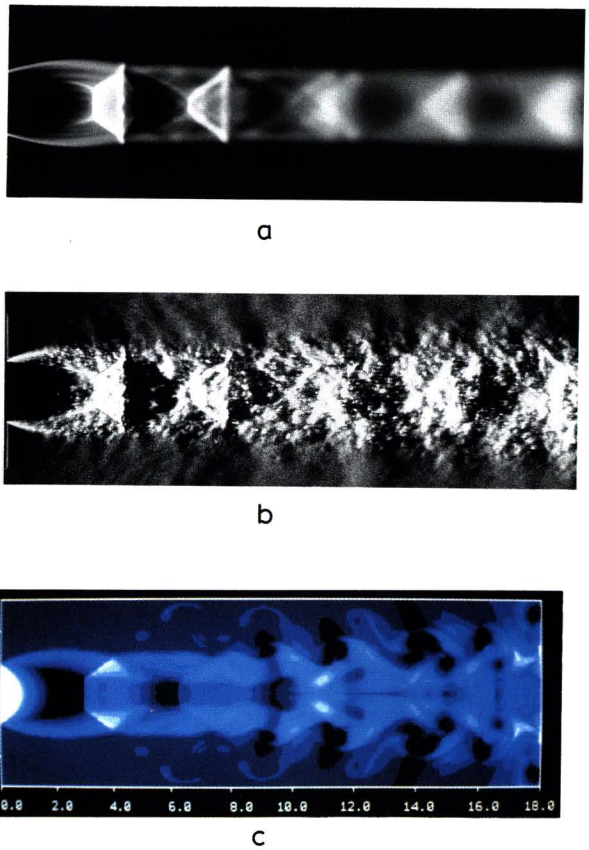

Fig 13. Same as Fig. 12, except the pressure ratio is $p_0/p_\infty = 5.84$ ($p_j/p_\infty = 3.09$).

In Figs. 12 and 13, the instantaneous photograph, the long-time-exposure photograph and the computed density of jets are shown for $p_0/p_\infty = 1.94$ and 5.84 ($p_j/p_\infty = 1.05$ and 3.09), respectively. As can be seen in Fig. 12, the flow structure for the lowest pressure ratio is the most unstable. On the jet boundary near the nozzle exit, the Kelvin-Helmholtz nonlinear wave is found. This wave is amplified to form the eddy systems (large ring vortices), which are convected downstream and interact with the shock-cell structure near the rear edge producing strong pressure waves. Some of these ring vortices merge together to form a larger ring vortex.

The shock-cell pattern in the case of $p_0/p_\infty = 5.84$ is more stable than the case of 3.90. This is probably because there is not enough time for the perturbation in the faster jet to increase.

6. Conclusion

An axisymmetric Euler equation was solved to obtain the time dependent flow patterns of underexpanded axial jets using the second-order explicit Osher scheme. The numerical results were compared with the experiment.

First, our numerical code was tested to see if it could give the proper characteristics of the first Mach disk measured by Love it al.[10] A satisfactory agreement was obtained.

Various kinds of numerical boundary conditions were tested and compared. A spacetime diagram of the density along the jet axis was used to measure the stability of the flows computed. As far as the side wall boundary is concerned, the ambient gas condition proposed by Sawada et al.[6] gives the best result, since the pressure waves formed at the downstream region are absorbed by the wall. On the other hand, the pressure condition at the side wall gives a reflection of waves and perturbs the flow. In this case, an oscillation of the first shock-cell structure can not be damped.

Regarding the downstream boundary, the ambient gas condition gives a clear and a regular shock-cell pattern, although a standing shock exists just in front of the boundary. We performed an experiment to insert an obstacle into the jet to obtain a more regular flow.

We restricted our attention mainly to a jet with the pressure ratio $p_j/p_\infty = 2.06$, and a time evolution of the flow was computed using the 450×74 cylindrical grid. In the early stage of the evolution, the unsteady motion of the head of the jet was observed, and it was compared with Norman et al.'s calculation[1-3]. A qualitative agreement was obtained.

At a later stage of the evolution, it was found that the flow did not settle

into a steady state. Ring vortices (Kelvin-Helmholtz roll-up) were formed successively at the jet boundary, and they were convected downstream. A ring vortex forms an effective de Laval nozzle, and a normal shock results near the nozzle throat. These shocks are convected downstream with the ring vortices.

In order to find an experimental counterpart of these numerical results, we took two kinds of schlieren photographs, i. e., a long-time-exposure one and an instantaneous one. In the instantaneous schlieren photograph, we observed a very turbulent flow with vortices and shocks. On the other hand, the long-time -exposure schlieren photograph gave a rather smooth shock-cell structure, and this represented a time averaged flow. We produced a time averaged flow, based on the numerical results, which shows a regular shock-cell structure.

A feedback loop producing disturbances in the flow field was discussed. Pressure waves (sound waves) are generated at the rear edge of the cellular structures by the interaction of ring vortices with the shock-cell structure, or by the impingement of the vortices with the outflow boundary. These waves propagate upstream and interact with the jet boundary to disturb it and form nascent ring vortices.

In the present calculation we restricted ourselves to an axisymmetric flow. As the instantaneous schlieren photographs show, three dimensional motions can not be neglected in some cases. In a future work such an effect will be included.

Acknowledgement

The computations were performed by the Fujitsu VP 200 vector processor at the Data Processing Center of Kyoto University and by the Fujitsu VP 50 at the Nobeyama Radio Observatory. This work was supported by the Grant-in-Aid for Scientific Research (61540183) of the Ministry of Education and Culture in Japan.

References

1. Norman, M. L., Smarr, L., Winkler, K.-H. A. & Smith, M. D., "Structure and Dynamics of Supersonic Jets", Astron. Astrophys., **113**, 1982, pp. 285 - 3.2.
2. Norman, M. L., Winkler, K.-H. A. & Smarr, L., "Propagation and Morphology of Pressure -Confined Supersonic Jets", in 'Astrophysical Jets' Ed. Ferrani, A. & Pacholczyk, A. G., D. Reidel, 1983, pp. 227 - 251.
3. Smarr, L., Norman, M. L. & Winkler, K.-H. A., "Shocks, Interfaces, and Patterns in Supersonic Jets", Physica, **12 D**, 1984, pp. 83 - 106.
4. Blandford, R. D. & Rees, M. J., "A 'Twin-Exhaust' Model for Double Radio Sources", Mon. Not. R. Astr. Soc., **169**, 1974, pp. 395 - 415.
5. Van Dyke, M., "An Album of Fluid Motion", The Parabolic Press, Stanford, 1982, p. 170.

6. Sawada, K., Shima, E., Matsuda, T. & Inaguchi, T., "The Osher Upwind Scheme and its Application to Cosmic Gas Dynamics", Mem. Fac. Eng. Kyoto Univ., **48**, 1986, pp. 240 - 264.
7. Osher, S. & Chakravarthy, S. R., "Upwind Schemes and Boundary Conditions with Applications to Euler Equations in General Geometries", J. Comp. Phys. **50**, 1983, pp. 447 - 481.
8. Chakravarthy, S. R. & Osher, S., "Numerical Experiments with the Osher Upwind Scheme for the Euler Equations", AIAA J., **21**, 1983, pp. 1241 - 1248.
9. Van Albada, G. D., Van Leer, B. & Roberts, W. W. Jr., "A Comparative Study of Computational Methods in Cosmic Gas Dynamics", Astron. Astrophys., **108**, 1982, pp. 76 - 84.
10. Love, E. S., Grigsby, C. E., Lee, L. P. & Woodling, M. J., "Experimental and Theoretical Studies of Axisymmetric Free Jets", NASA Technical Report **R-6**, 1959.
11. Powell, A., "On the Noise Emanating from a Two-Dimensional Jet Above the Critical Pressure", Aeronautical Quarterly, **4**, 1953, pp. 103 - 122.
12. Powell, A., "On the Mechanism of Choked Jet Noise", Proc. Phys. Soc. London B, **66**, 1953, pp. 1039 - 1056.